Available online at www.sciencedirect.com

SciVerse ScienceDirect

journal homepage: www.elsevier.com/locate/he

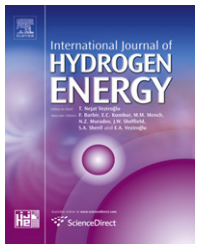

Flame chemiluminescence and OH LIF imaging in a hydrogen-fuelled spark-ignition engine

P.G. Aleiferis, M.F. Rosati*

Department of Mechanical Engineering, University College London, Torrington Place, London WC1E 7JE, UK

ARTICLE INFO

Article history:
Received 17 July 2011
Received in revised form
1 October 2011
Accepted 4 October 2011
Available online 26 October 2011

Keywords:
Spark ignition engines
Hydrogen combustion
Flame chemiluminescence
OH Laser Induced Fluorescence

ABSTRACT

Research into novel internal combustion engines requires consideration of the diversity in future fuels in an attempt to reduce drastically CO_2 emissions from vehicles and promote energy sustainability. Hydrogen has been proposed as a possible fuel for future internal combustion engines. Hydrogen's wide flammability range allows higher engine efficiency with much leaner operation than conventional fuels, for both reduced toxic emissions and no CO_2 gases. This paper presents results from an optical study of combustion in a spark-ignition research engine running with direct injection and port injection of hydrogen. Crank-angle resolved flame chemiluminescence images were acquired and post-processed for a series of consecutive cycles in order to calculate in-cylinder rates of flame growth. Laser induced fluorescence of OH was also applied on an in-cylinder plane below the spark plug to record detailed features of the flame front for a series of engine cycles. The tests were performed at various air-to-fuel ratios, typically in a range of $\varphi = 0.50–0.83$ at 1000 RPM with 0.5 bar intake pressure. The engine was also run with gasoline in direct-injection and port-injection modes to compare with the operation on hydrogen. The observed combustion characteristics were analysed with respect to laminar and turbulent burning velocities, as well as flame stretch. An attempt was also made to review relevant hydrogen work from the limited literature on the subject and make comparisons were appropriate.

1. Introduction

1.1. Background

1.1.1. Hydrogen fuelling

Hydrogen has been suggested as a possible replacement for most fuels used today and can be produced from sustainable methods. The main advantage of burning hydrogen in internal combustion engines is its lack of carbon content, leading locally to no exhaust emissions of particulate matter, unburned hydro-carbons, CO and CO_2. The concept of an internal combustion engine running on pure hydrogen is as old as the engine itself. However, the lack of established technology necessary to handle some issues related to the properties of hydrogen, as well as the diversity of political opinions and projected infrastructure costs for the safe production and delivery of hydrogen on a large scale, have discouraged most automotive manufacturers from promoting hydrogen as a fuel for their engines. Nevertheless, sustainability issues and impeding stricter exhaust emissions legislation have made hydrogen the subject of much discussion, with new research for fundamental understanding of in-cylinder phenomena in hydrogen combustion systems critically needed.

* *Corresponding author*. Tel.: +44 (0) 20 76793862; fax: +44 (0) 20 73880180.
E-mail address: p.aleiferis@ucl.ac.uk (P.G. Aleiferis).
0360-3199/$ – see front matter
doi:10.1016/j.ijhydene.2011.10.010

Nomenclature

p	Pressure
T	Temperature
u'	Turbulence intensity
u_l	Laminar burning velocity
u_t	Turbulent burning velocity
ϕ	Equivalence ratio

Abbreviations

AFR	Air-to-Fuel Ratio
AIT	After Ignition Timing
ATDC	After intake Top Dead Centre
BDC	Bottom Dead Centre
BTDC	Before Compression TDC
CA	Crank Angle
CFD	Computational Fluid Dynamics
COV	Coefficient of Variation
DI	Direct Injection
DISI	Direct Injection Spark Ignition
EGR	Exhaust Gas Recirculation
ETU	Engine Timing Unit
EVC	Exhaust Valve Closure
EVO	Exhaust Valve Open
LDV	Laser Doppler Velocimetry
LIF	Laser Induced Fluorescence
IMEP	Indicated Mean Effective Pressure
IVC	Intake Valve Closure
IVO	Intake Valve Open
MBT	Minimum spark advance for Best Torque
MFB	Mass Fraction Burned
PFI	Port Fuel Injection
PIV	Particle Image Velocimetry
PM	Particulate Matter
RPM	Revolutions Per Minute
SI	Spark Ignition
SOI	Start of Injection
TEA	TriEthylAmine

1.1.2. *Hydrogen properties*

A general review of the research done on hydrogen as a fuel for automotive applications up to the mid 90's has been given by Norbeck *et al.* [1]. More recent reviews have been published by White *et al.* [2] and Verhelst *et al.* [3,4] and Verhelst and Wallner [5].

Some of hydrogen's properties, particularly relevant to in-cylinder mixture formation and combustion, are summarized in Table 1 in comparison to those of gasoline and methane [6–8]. Hydrogen has very low density and, although its heating value on a mass basis is very high in comparison to other fuels (120 MJ/kg for hydrogen, 43.5 MJ/kg for gasoline), on a volume basis this is the lowest among common fuels (10.2 MJ/m^3 for hydrogen, 216.4 MJ/m^3 for gasoline). Hydrogen's minimum ignition energy is about one order of magnitude less than that of gasoline; hydrogen also has a small quenching distance which means that hydrogen can autoignite easily and its flame can get past a nearly closed intake valve more readily and backfire into the intake manifold. Additionally, NO_x emissions from stoichiometric combustion of hydrogen are comparable to those from engines fuelled by gasoline or common gaseous fuels. However, hydrogen has a wide range of flammability, hence it is possible to burn it in much leaner/cooler flames than gasoline or natural gas, *i.e.* with Air-to-Fuel Ratio (AFR) greater than the stoichiometric or, differently, for ϕ = AFRstoic/AFR<1. This leads to quite low NO_x emissions, especially for $\phi < 0.5$; Exhaust Gas Recirculation (EGR) can also be used to control the combustion duration, knocking and NO_x emissions in SI hydrogen engines [9–13].

1.1.3. *Hydrogen injection*

Particularly due to pre-ignition/backfire and NO_x-related problems, injection systems and mixture preparation strategies for hydrogen engines have attracted a lot of attention. However, no commercial injectors have been fully developed yet specifically for the life-cycle of a hydrogen engine because much larger volumes of fuel must be injected per stroke due to the very low density of hydrogen; hydrogen's low lubricity also leads to severe durability problems for injectors that have been designed for common fuels [14]. Nevertheless, commercially available Port Fuel Injection (PFI) systems for common gaseous fuels can be adopted for engine operation

Table 1 – Properties of Hydrogen, Gasoline and Methane.

Parameter	Hydrogen	Gasoline	Methane
Density [kg/m^3]	0.09 (0 °C) 71 (−253 °C)	5.1 (vapour) 730–780	0.72 (0 °C) 423 (−162 °C)
Stoichiometry [kg_{Air}/kg_{Fuel}]	34.3	14.7	17.2
Lower Heating Value [MJ/kg]	120	43.5	50
Lower Heating Value at $\phi = 1$ [MJ/kg]	3.40	2.83	2.72
Boiling Temperature [°C]	−253	25–215	−162
Ignition Limits [Volume%, ϕ]	4–75, 0.1–6.67	1.0–7.6, 0.71–2.5	5.3–15, 0.48–1.43
Minimum Ignition Energy at $\phi = 1$ [mJ]	0.02	0.24	0.29
Autoignition Temperature [°C]	585	350	540
Quenching Distance [mm]	0.64	2.0	2.03
Kinematic Viscosity [m^2/s]	110×10^{-6}	1.18×10^{-6}	17.2×10^{-6}
Thermal Conductivity [W/m K]	182.0×10^{-3}	11.2×10^{-3}	34.0×10^{-3}
Diffusion Coefficient in Air [m^2/s]	6.1×10^{-5}	0.5×10^{-5}	1.6×10^{-5}

with hydrogen for research and/or demonstration purposes that do not entail long running engine times. However, with PFI, even if one uses strategies to prevent backfire by retarding the injection (such that the end of injection is timed to occur just prior to intake valve closure) and running lean ($\phi < 0.50$) the in-cylinder charge has about 18% lower calorific value at stoichiometric conditions than a gasoline-air mixture (due to air displacement from the large volume of injected hydrogen) which leads to a large power deficit and the requirement to supercharge the engine [15,16]. Hence, adoption of hydrogen DI systems seems to offer certain potential because hydrogen can be typically injected when the intake valves have already closed, therefore, backfire is not an issue and no air is displaced during injection.

1.2. *Optical diagnostics*

Although various technical problems of hydrogen SI engines have been tackled and solved in an empirical manner, little work has been published on optical diagnostics of hydrogen combustion in modern engine designs. Heywood and Vilchis [17] used Schlieren imaging to compare propane and hydrogen combustion in a square section optical SI engine. They showed that the propane and hydrogen flames fell in different regimes because the hydrogen turbulent flame thickness was about one third to one quarter that of propane, whilst the speed of burning for hydrogen was much faster than that of propane. Meier *et al.* [18] used Raman Scattering in a DI hydrogen SI engine and reported that the quality of mixing was not affected by injection timing which was attributed to the high diffusivity of hydrogen. However, Rayleigh scattering and Schlieren imaging have shown that high injection pressures can lead to hydrogen concentrations beyond the ignitability limit [19]. Meier *et al.* [20] used a Schlieren system to visualise hydrogen-air mixture formation in an SI engine and calculated that the flame speeds obtained with internal mixture formation were significantly higher than those with external mixture formation. Laser Induced Fluorescence (LIF) techniques, based on acetone or other fuel dopants, have recently been developed particularly for the study of mixture formation in hydrogen engines with DI systems [21,22]. Additionally, recent studies involving application of acetone LIF and Particle Image Velocimetry (PIV) in DI hydrogen engines have provided some insights into the interactions between the jets of hydrogen injection and the in-cylinder flow field. Some of these studies are discussed below in more detail because of their direct relevance to the in-cylinder phenomena of the engine geometry employed in the current work.

1.2.1. *Hydrogen mixture formation in DI engines*

White [23,24] presented flame chemiluminescence and acetone-LIF images from a hydrogen-fuelled optical engine, employing high (100 bar) and low (25 bar) injection pressures, studying its effect on different timings of Start Of Injection (SOI). He concluded that for pre-Intake Valve Closure (IVC) injection and SOI coincident with IVC, a near-homogeneous mixture distribution was observed and there were little differences between the two injection pressures studied. With moderate retard of SOI from IVC, higher injection pressure improved in-cylinder mixing. With late injection and both injection pressures, hydrogen was predominately concentrated in small volumes located towards the cylinder walls. In further research using acetone LIF, Salazar *et al.* [25,26] studied different multi-hole injector nozzle geometries and showed that for early injection, the low in-cylinder pressure and density allowed the hydrogen jets to preserve their momentum long enough to undergo extensive jet-wall and jet-jet interactions, but the final mixture was fairly homogeneous. Intermediately-timed injection yielded inhomogeneous mixtures with surprisingly similar features observed for all injectors, with fuel mostly concentrated near the cylinder wall. Results for late injection depended more on injector configuration. Single-hole injection tests showed that neither changing the nozzle orientation nor increasing the intake-induced tumble resulted in drastic modifications of mixture formation. This was attributed to the spatially concentrated momentum input by the single-hole injector operated at high-fuel pressure. Lower pressure or multi-hole injectors were expected to lead to greater sensitivity to interaction with the bulk flow. Kaiser *et al.* [27] employed acetone LIF in synergy with PIV to characterise the interaction of the hydrogen jets with the in-cylinder flow for different charge preparation strategies. It was concluded that, for early injection, fuel and cylinder charge were essentially premixed; intermediate and late injection yielded bi-modal distributions of the fuel mass across equivalence-ratio space, with a rich region near the injector and lean mixtures throughout the rest of the field of view. Rich and lean regions were separated by a mixing region with large turbulence intensity in the PIV images. The PIV vector plots acquired for the three post-IVC injection timings showed that the injection event significantly changed the in cylinder flow field compared to the non-fuelled flow field.

1.2.2. *Hydrogen's burning velocity*

Some of the first measurements of hydrogen's burning speed at elevated temperatures and pressures have been published by Milton and Keck [28]. In a recent publication, Bradley [29] presented a review of the effect of different physical and chemical properties of various fuels on laminar burning velocities, Markstein numbers, flame extinction rates for positive and negative stretch, as well as turbulent burning rates, including some reference to hydrogen. Earlier work by Bradley *et al.* [30], specifically on hydrogen explosions in a combustion bomb, had discussed the difficulties associated with the quantification of unstretched laminar burning velocities for hydrogen at engine-like conditions (1–10 bar, $\phi = 0.3$–1.0) due to the appearance of Darrieus-Landau and thermodiffusive instabilities soon after ignition that enhance hydrogen's flame speed. Law *et al.* [31] characterised hydrogen-propane/air expanding flames at high pressure through both experiments and theoretical analysis. Critical conditions for the onset of instability were measured for $\phi = 0.6$–0.9 at 5 bar, 300 K and those were in good agreement with Bradley's work [30]. Wu *et al.* [32,33] used a turbulent jet burner to measure turbulent burning velocities u_t for hydrogen/air mixtures with various equivalence ratios. The measurements not only showed an increase in u_t for unstable mixtures, but also a 'dampening' of turbulent fluctuations and

thus a decrease of u_t for stable mixtures. Later, Aung *et al.* [34,35] reported measurements of flame speed in a fan-stirred bomb. Mixtures of hydrogen, nitrogen and oxygen were prepared with almost identical laminar burning velocities but different thermo-diffusive stability (stable/neutral/unstable) and mixtures of propane/air with similar u_t but varying stability. Again, u_t clearly increased for unstable mixtures. Both measurements on the burner and the bomb showed strong dependence of u_t on mixture stability even for strong turbulence.

1.3. *Present contribution*

Very little work has been published in optical engines with respect to in-cylinder hydrogen burning rates, especially in direct comparison with gasoline combustion in the same engine. Previous work by the current authors focused on high-speed flame chemiluminescence imaging of hydrogen combustion under spark ignition and controlled autoignition (or Homogeneous Charge Compression Ignition, HCCI) operation in an optical engine [36]. The present work aims to provide and discuss further combustion data from the same optical engine fuelled with either hydrogen or gasoline in spark-ignition mode of operation, and to characterise combustion by:

- High-speed imaging of flame chemiluminescence over a series of consecutive engine cycles.
- Imaging of hydrogen's flame structure by Laser Induced Fluorescence of OH.
- Studying the effect of DI and PFI mixture formation strategies on in-cylinder burning phenomena.
- Comparing the flame speeds derived from combustion imaging with previous studies on other hydrogen engines, as well as from combustion 'bombs', under laminar or turbulent conditions.

The current work is believed to contribute towards a database of hydrogen combustion rates which are essential for developing our knowledge of the underlying fundamental mechanisms under realistic engine conditions. Such data can also assist modellers because simulation of hydrogen combustion from an engine designer's perspective can be quite challenging. This paper also makes an attempt to review and discuss relevant information from the literature and to provide an analysis framework in the context of both simplified combustion experiments and DISI engines running on hydrogen.

2. Experimental apparatus and procedure

2.1. *Optical engine*

The engine used in this study was a single-cylinder research engine designed and built at University College London (UCL). The bore of the engine was 89 mm and the stroke was 79 mm; the compression ratio was 7.5. Geometrical properties of the engine, along with other specifications are summarised in Table 2. A hollow 'Bowditch' piston allowed for a 45° stationary mirror to be fitted inside the block in order to gain optical access to the combustion chamber through a quartz piston crown. A vacuum pump was connected to the crankcase to draw oil-laden gas out and reduce smearing of the mirror and the piston crown. The engine design also accommodated a pentroof window and side full stroke window for optical access through the liner. However, it was only the piston optical crown and the small pentroof window, that were retained for the current study due to uncertainties involved with the thermal stressing of the engine when run with hydrogen fuelling.

Table 2 – Engine Specifications.

Engine Type	4-Stroke, Single-Cylinder Optical
Engine Head	4-Valve Pentroof (Prototype V8)
Piston shape	Flat
Bore/Stroke [mm]	89/79
Displacement [cm^3]	498
Injection System	PFI, DI
Valve Timings [°CA AITDC]	IVO 706, IVC 216, EVO 506, EVC 16

Engine control was achieved by using shaft encoders, with a resolution of 1800 pulses per revolution, fixed to the engine's camshafts and crankshaft, as well as an AVL 427 Engine Timing Unit (ETU). The encoder also fed a Top Dead Centre (TDC) reference to the ETU.

The intake manifold was fed by an air plenum chamber of 100 lt capacity via a 2 m long pipe. A standard throttle and airflow meter were positioned at the inlet pipe to the plenum chamber. The intake pressure was monitored by a Druck PMP1400 piezo-resistive absolute pressure transducer whose analogue output was fed to a LabVIEW-based data acquisition system. The engine's head and block were heated via an independent water circulation system and heat exchanger. The engine speed was set to 1000 RPM. The engine temperature was set to 85 °C to represent typical warm running engine conditions. The load was set by the throttle to 0.5 bar intake manifold pressure to enable typical part-load engine operation. Particular care had to be taken when running the optical engine on hydrogen at 1.0 bar intake pressure close to stoichiometry due to the large peak in-cylinder pressures achieved, hence no tests were carried out at this operating point with either gasoline or hydrogen within the objectives of the current work. A schematic of the test bed is given in Fig. 1.

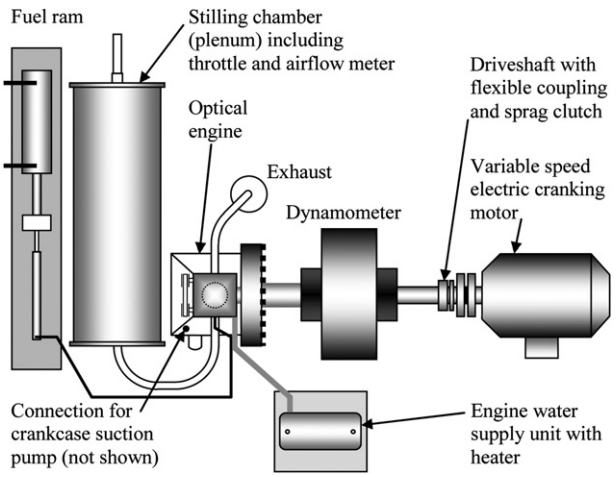

Fig. 1 – Engine Test Bed Arrangement.

2.2. Fuel supply systems and injectors

The engine accommodated a fully flexible fuelling system, capable of both PFI and DI of liquid and gaseous fuels. Three injectors were fitted on the engine, two on the intake ports allowing for simultaneous injection of liquid and gas fuels and one in-cylinder for DI engine operation. A standard Bosch single-hole fuel injector was used for the PFI gasoline system. Hydrogen was injected in the intake port using a Keihin KN3-2 gas injector. Selection of the injector for the DI fuelling system was not trivial. The engine head had been originally designed to operate with a side gasoline pressure-swirl atomizer at 45° inclination located between the intake valves. One of the requirements of the DI system for the current work was to allow flexibility for use with both liquids and gases and a multi-hole injector was finally selected. The injector nozzle had a 6-hole arrangement that consisted of two groups of 3 asymmetric holes originally designed for a spray-guided DI gasoline combustion system with vertically mounted injector in close-spacing arrangement with the spark plug. This was a cost-effective choice able to cope with the high flow-rate requirements needed for hydrogen. However, it must be pointed out that it was only due to the short running periods involved with optical engine operation that it was possible to adopt safely such a solution (hydrogen's low lubricity would not allow the injector to live long). The position of the injector and its nominal spray pattern with respect to the combustion chamber are shown in Fig. 2. Due to the asymmetry of the nozzle-hole pattern, after several tests of the engine's operation stability, an orientation with the two sets of plumes pointing upwards towards the pent-roof was finally adopted as shown in Fig. 2.

Hydrogen was supplied by pressurized bottle using two distinct pressure regulators, typically set to 70 bar for DI and to 4 bar for PFI work. The fuel supply system also comprised a back-flash arrestor, a micrometric in-line filter and a mass-flow controller (Bronkhorst F-203AC). The latter was calibrated by the manufacturer for hydrogen operation and connected via a serial cable to a PC in order to monitor and control the fuel flow to the injector in real time. Higher injection pressures may have been more beneficial for hydrogen DI in order to shorten the injection pulses whilst providing the engine with the required mass-flow within an appropriate crank-angle 'window' of the thermodynamic cycle; however, the selected pressure was the highest permitted by the gas mass-flow controller. To measure AFR directly, provision was made in the exhaust manifold for a heated wide-range exhaust gas oxygen (UEGO) sensor which allowed for multi-fuel calibration. Data from the hydrogen mass-flow controller provided a cross check of the AFR value.

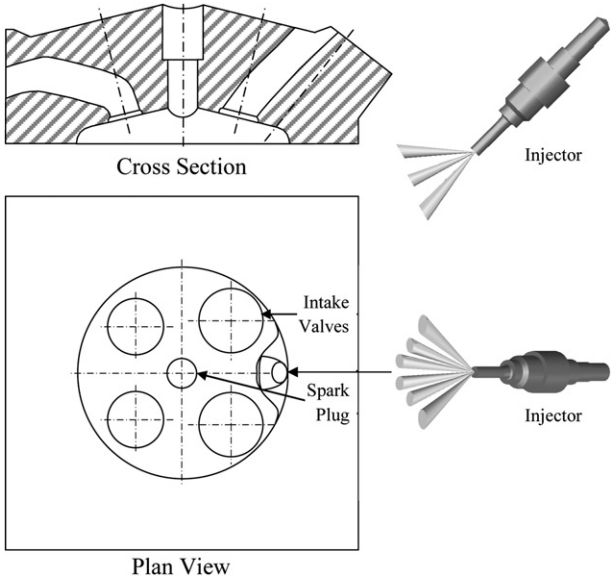

Fig. 2 – Combustion Chamber Geometry and Orientation of Injector with Nominal Spray Pattern.

The engine's valve timing strategy was one of advanced Intake Valve Closing (IVC) and retarded Exhaust Valves Opening (EVO), leading to 6.5° CA positive valve overlap (shown in Table 2). The residual gas fraction in the engine was calculated by modelling the engine's operation using geometrical and valve timing data via the detailed methodology offered by the Lotus engine simulation software [37] and was found to be 22%. It should be noted that in this paper 0° CA corresponds to Intake Top Dead Centre (TDC) and crank angles will be mainly presented with respect to that as °CA After intake TDC (ATDC). Various injection strategies with different Start of Injection (SOI) timings were used, as will be discussed later.

2.3. Ignition system

The ignition system was of standard coil and driver type. The dwell time was set to 3 ms to limit the electronic noise on the data acquisition system. The spark plug was a Bosch Platinum with quadruple electrode, the orientation of which within the combustion chamber was established by the thread pattern of the plug. It was energised using a standard coil attached to a 12 V power supply and spark timing was controlled by TTL from the AVL engine timing unit.

Initial tests were carried out to identify suitable ignition timings by mapping the engine and establishing the Minimum spark advance for Best Torque (MBT) for each fuel used and injection system. Engine mapping showed that MBT timings were in the range of 30–40° CA Before compression TDC (BTDC) for gasoline with fuelling in the range at $\phi = 0.83–1.0$ and 8–18° CA BTDC for hydrogen with fuelling in the range $\phi = 0.50–0.83$. Typically the ignition timing was set to 325° CA ATDC (*i.e.* 35° CA BTDC) for gasoline and 325° CA ATDC (*i.e.* 15° CA BTDC) CA for hydrogen. This was done for the purposes of direct comparison between combustion images of the same fuel at nominally same ignition timings because the effect of spark advance on engine output for fixed equivalence ratios was relatively flat around the chosen timings for most conditions studied.

2.4. Pressure measurements and analysis

The in-cylinder pressure measurements for the present study were conducted with a water-cooled piezo-electric pressure transducer (Kistler 6041A) specifically suited to engine applications due to its low temperature shock sensitivity and stable zero point. The transducer was connected to a Kistler 5011B10

charge amplifier and absolute pressure referencing was done via the mean intake manifold pressure.

The pressure signals were digitised on a cycle-to-cycle basis with a 12-bit analogue-to-digital converter (National Instruments PCI-MIO-16E-4) within LabVIEW at a resolution of 0.4° CA at 1000 RPM. The uncertainty due to electrical interference was a maximum of 0.05% of the full scale value for the in-cylinder pressure and 1% of full scale value for the intake plenum and barrel pressures, corresponding to an uncertainty of ±5.0 mbar and ±10 mbar, respectively. Thermodynamic analysis was done on the pressure traces with MATLAB-based software to calculate IMEP, rates of heat release and Mass Fraction Burned (MFB) using methods published in [38–40]. The errors involved in acquiring and processing were carefully considered. The effects of numerical integration associated with calculating IMEP can be minimised provided the crank angle resolution is smaller than 1° CA; according to [41] a ±0.5° CA uncertainty in the phasing of TDC gives ±2.5% uncertainty in IMEP. Errors will also arise from the effects of signal noise, accurate definition of con-rod length and the correct phasing of TDC with pressure. In the current arrangement the accuracy of the con-rod length was accurate to below 0.01% and the position of TDC was accurate to within less than ±0.1° CA such that errors in IMEP and mass fraction burned due to the experimental arrangement were considered to be negligible.

2.5. *High-speed chemiluminescence imaging*

A high-speed CMOS camera (Photron APX-RS) was used for crank-angle resolved chemiluminescence imaging. Specifically, the camera was employed at a frame rate of 3 and 6 kHz, corresponding respectively to 2° and 1° CA between frames at 1000 RPM. This was done for image sizes of 640 × 480 pixels, giving a resolution of 160 μm per pixel. No filters were used in order to capture broadband light emission. However, a detailed spectroscopic study was undertaken in parallel [42] and this will be reported in a future publication. The camera memory allowed over 100 cycles of data with 50 frames per cycle to be acquired consecutively before data-download to a PC was necessary. It was nevertheless considered safer to image the combustion for exactly 100 consecutive cycles each time to avoid excessive stresses on the quartz windows of the engine. Synchronization of various control triggers for ignition, injection and camera was achieved using the optical encoder on the camshaft as engine clock connected to the AVL Engine Timing Unit. Once image acquisition was complete, images were downloaded from the camera via IEEE 1394 FireWire to a PC system for image storage as 8-bit Tagged Image File Format (TIFF) files in 256 greyscales.

In order to obtain quantitative information from the combustion images flame areas were obtained on a cycle-by-cycle basis via thresholding/binarisation of each flame image to define the 'projected' in-cylinder enflamed area by summing up the pixels that had intensity higher than a threshold. Great care was exercised to define an appropriate circular region of interest on the flame images in order to isolate the flame-only chemiluminescence without picking up any light from reflections at the boundaries of the circular window of the piston crown. The methodology was checked 'on-line' for each processed flame to ensure that visually the flame areas were being faithfully reproduced for the whole period of flame growth. Mean flame growth curves were plotted for all fuels in terms of an 'equivalent radius' calculated from the flame areas of all individual cycles based on the area of a circle equal to the flame area measured from each image. The flame radius was used as an additional metric to MFB since it typically reveals details about flame growth during the early stages of heat release on a cycle-by-cycle basis (usually 0–5%), a period which is typically not resolved well by thermodynamically derived MFB data. Flame speeds were inferred from flame radii by using a finite-difference approach and plotted both in time and against flame size.

Uncertainties in the calculated ensemble averaged flame area were estimated by considering a single binarised flame. The area calculated for this flame was compared to the area of the same flame with an extra pixel added to the equivalent flame radius. This was considered to represent an uncertainty linked to the spatial resolution of the imaging arrangement. Second, the change in the binarised area of a flame due a change in the threshold value was also computed. For small flames, *e.g.* at ~10° CA AIT with gasoline fuelling, these uncertainties were found to be ±9% and ±0.2–0.4% per threshold unit of the nominal equivalent flame radius, respectively, the latter reflecting clearly the low sensitivity of the threshold value to the flame area calculation in the early stages of combustion. For larger flames, *e.g.* at ~30° CA AIT with gasoline fuel, considering a wider window of uncertainty due to the higher flame luminosity of ±5 pixels the uncertainties were still found to be quite low, ±0.5–2% and ±1–2% of the equivalent flame radius, respectively. Given that the cycle-to-cycle variations in flame development for gasoline combustion had a Coefficient of Variation (COV) of the equivalent flame radius of ~50–60% (with COV of IMEP stable at ~3%) and 20% for hydrogen combustion (with COV of IMEP stable at 2%), these uncertainties were not expected to influence the categorisation of mean flame growth rates for different conditions.

2.6. *OH Laser Induced Fluorescence*

The pump laser was a Continuum Surelite III Nd:YAG. In order to obtain light of 532 nm the second harmonic was used. The beam was then steered into a Sirah Cobra Stretch dye laser. It was chosen to excite rotational lines of the transition $A^2\Sigma^+$ ($v' = 1$) ← $X^2\Pi$ ($v'' = 0$) which were deemed those capable of strong signals, hence the excitation wavelength required from the dye laser had to be in the range from 279.00 to 291.00 nm. Rhodamine 6G dye was employed; its lasing range has close proximity to its absorption maximum (approximately 530 nm). The light coming from the excited dye, or fundamental wavelength at 566 nm, crossed a frequency doubler again, resulting in a maximum output at ~283 nm, which is optimal when seeking rotational lines in the range cited earlier. The lines in the range from 284 to 281 nm were the ones which yielded the strongest signals and the rotational line at 282.90 nm was finally selected after fine tuning. Energy of the order 400 mJ per pulse was necessary from the Nd-YAG to obtain ~25 mJ max per pulse from the dye laser. The mirrors adopted to drive the beam exiting the dye laser beam were Techspec Nd:YAG Laser 266 nm with near 100% reflection at the wavelengths adopted. The sheet maker was

a LaVision cylindrical F/20 lens with embedded focusing mechanism. The shape resulting from this arrangement was a 0.5 × 60 mm laser sheet, entering the engine 1 mm above the combustion deck.

The camera employed for OH LIF was a Princeton Instruments Intensified Charge Couple Device (ICCD), PI-MAX camera with an array size of 512 × 512 pixels. The camera was fitted with a P43 photocatode for maximum efficiency in the UV. 100 ns gating was employed as this was compatible with the typical timings involved with an internal combustion engine. A Nikon 105 mm f/4.5 UV lens was used to collect light coming from the combustion chamber via the UV enhanced mirror located in the hollow piston extension. The optical parts were realised in UV polished fused silica for both piston and side pentroof window. In order to resourcefully isolate the fluorescence signal from broadband chemiluminescence and block scattered light, a combination of Schott UG11 and Schott WG 305 filters was employed. The WG 305 filter was used to block all the light with wavelengths shorter than 305 nm, including all the scattering generated by the laser light at 293 nm. The UG 11 filter was employed to block most of the visible spectrum, allowing band-pass from 245 to 410 nm (peak at 340 nm). The pair of filters transmitted ~56% of the incident radiation in the band between 305 and 320 nm. In order to control the camera and Laser triggers with nanosecond precision, a Stanford Signal Generator was employed to finely adjust the pulses coming from the ETU. Fig. 3 shows the optical arrangement for OH LIF imaging. The intensifier was set to ~85% of its maximum gain to eliminate increased levels of digital noise at maximum nominal output.

3. Results and discussion

3.1. Flame expansion

3.1.1. General characteristics

Fig. 4 presents typical sets of crank-angle resolved flame development images for hydrogen PFI and DI, as well as gasoline DI, at part load (0.5 bar intake pressure) at different equivalence ratios. The injection timing was set for DI to SOI = 220° CA ATDC regardless of fuel (*i.e.* very close to the IVC), to 360° CA ATDC for PFI gasoline (*i.e.* injection against the hot closed intake valves at compression TDC) and to 0° CA ATDC for PFI hydrogen (*i.e.* against open intake valves at intake TDC). DI pressure was 70 bar for hydrogen and 100 bar for gasoline. The AFR investigated was in the range $\phi = 0.50–0.83$ to provide enough luminosity for combustion images of adequate quality whilst not overstressing the optical engine. It must be pointed out though that steady hydrogen combustion could be achieved with much leaner AFR (*e.g.* $\phi = 0.3$). The hydrogen DI images in Fig. 4 have not been post-processed in any fashion and the luminosity shown is the 'raw' flame chemiluminescence as recorded by the high-speed camera. However, the hydrogen PFI images and the gasoline images of Fig. 4 had to be boosted by ~20% in terms of brightness and contrast for printing and reproduction purposes. Therefore, although the amplitude of chemiluminescence is of comparable level across all images of Fig. 4, the hydrogen DI flames were brighter in raw intensity.

The hydrogen chemiluminescence images presented mostly flame shapes with small overall distortion from 'circular' development on a macro-scale. For PFI in particular, flame growth was typically symmetric in all directions with respect to the central location of the spark plug on a cycle-to-cycle basis; this is clearly shown from Fig. 4 for $\phi = 0.83$; some asymmetric expansion with deviations of the flame's shape from a 'circle' with more obvious wrinkling of the boundaries of the hydrogen flame started to appear with PFI for $\phi < 0.67$, but still this was not anywhere close to the asymmetric expansion and distortion of the flame boundaries observed for gasoline operation. For hydrogen DI, flame growth was very fast for $\phi = 0.83$; typically the expansion was relatively symmetric again but with more pronounced irregularities in the boundaries of the flame than with PFI. To put DI combustion phenomena into context with hydrogen-air mixing, it is worth mentioning that with an injection pressure of 70 bar at an engine load of 0.5 bar intake pressure, the

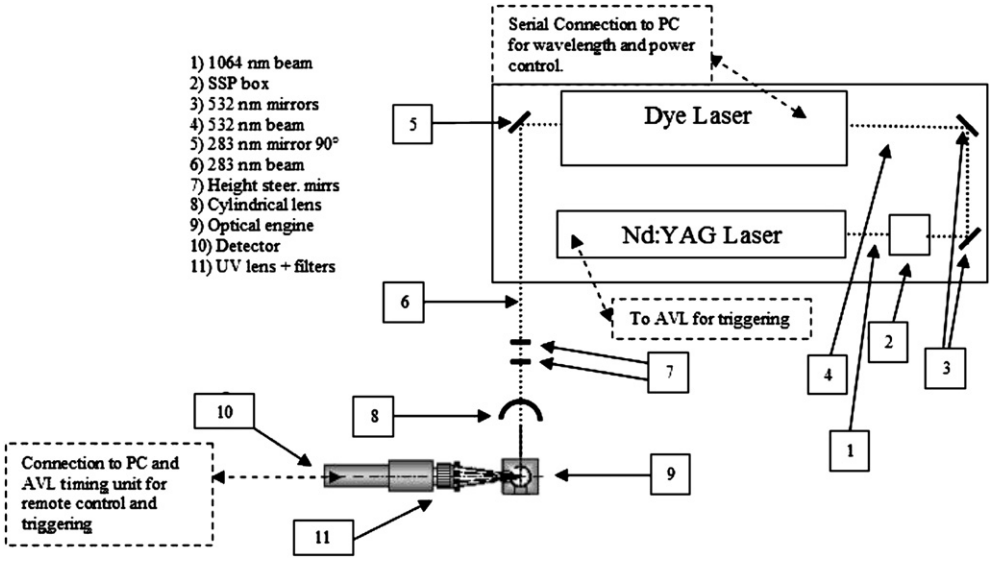

Fig. 3 – Setup for OH LIF.

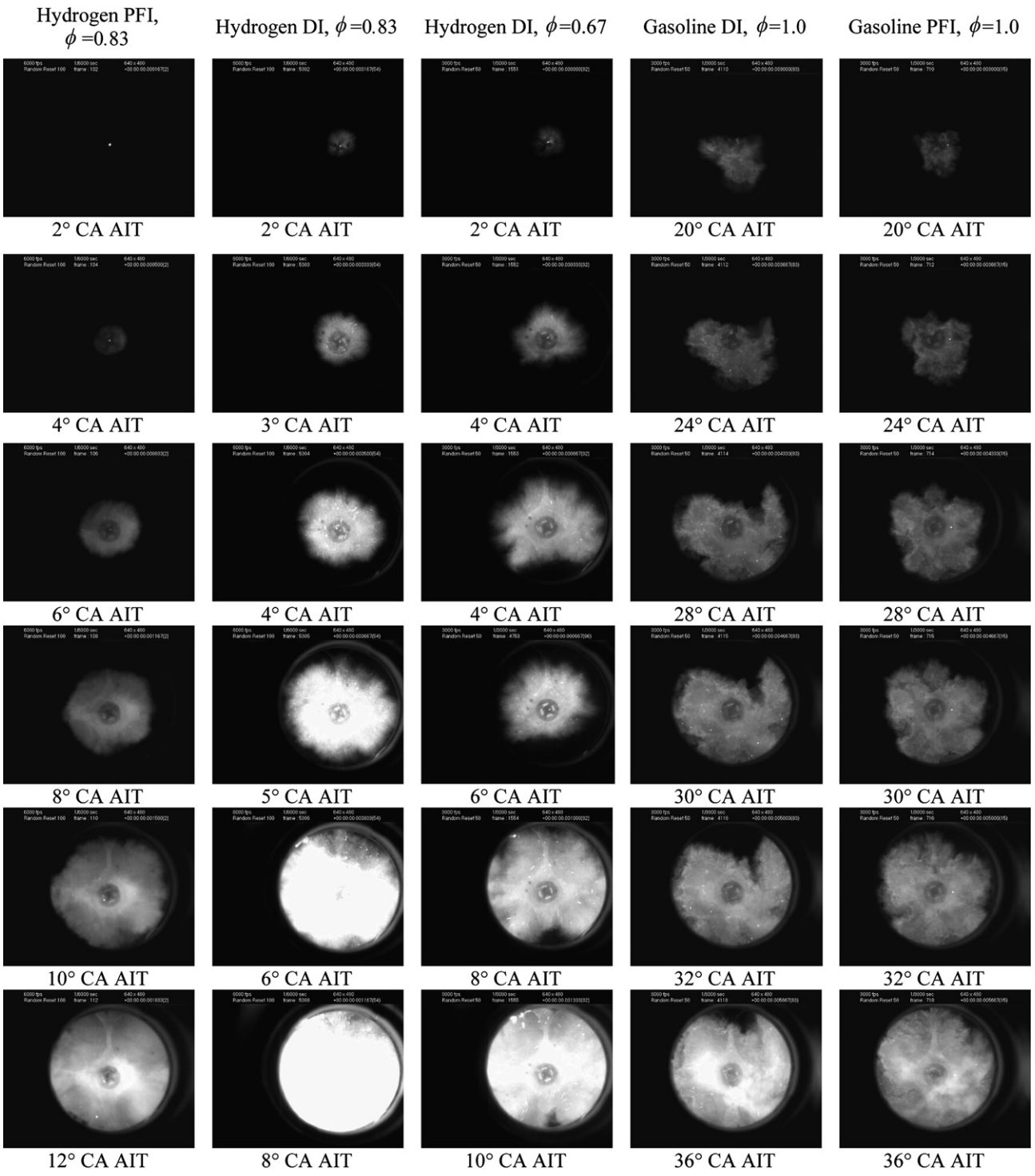

Fig. 4 – Flame Chemiluminescence: Hydrogen (DI & PFI), Spark Advance 15° CA; Gasoline (DI & PFI), Spark Advance 35° CA (Intake Valves at the Top, Exhaust Valves at the Bottom).

DI system required a pulse-width ranging from 4 to 6 ms, to fulfill fuel requirements at the equivalence ratios presented in Fig. 4 ($\phi = 0.50–0.83$). At 1000 RPM, 6 ms correspond to 36° CA. Considering that the injection timing started at 220° CA ATDC, there was about 89° CA after the end of injection for hydrogen to mix and lose most of its initial jet momentum before ignition timing for $\phi = 0.83$. For $\phi = 0.67$ DI hydrogen flame expansion remained symmetric on a macro scale but even more pronounced irregularities appeared on the flame boundaries as shown in Fig. 4; these could be attributed to the balance between in homogeneities in the mixture field and the turbulent scales since flame growth was quite slower than for $\phi = 0.83$ DI. With hydrogen DI, fuelling had to be decreased to values of $\phi < 0.6$ for flame expansion to be of the same speed

to that observed with hydrogen PFI at $\phi = 0.83$, as will be quantified later in this paper.

Overall it can be said that both DI and PFI hydrogen flame development was less sensitive to any of the parameters that affect the directionality of gasoline flame development, *e.g.* the presence of in-cylinder charge motion due to tumble and/or swirl flow macro-structures, as well as the temperature gradient between intake and exhaust side, that typically 'force' gasoline flames to follow specific paths of in-cylinder motion, mainly from the intake to the exhaust side. The average flame centroid displacement speed for gasoline combustion was of the order 4 m/s during the first 20–25° CA AIT, in agreement with previous work on the subject [38,40]. Hydrogen flame centroid displacement speeds were calculated in this work to be of the order ~2 m/s for $\phi = 0.67$–0.83, with PFI exhibiting even smaller values. A Schlieren study of hydrogen flame motion on the vertical plane of an optical SI engine for different levels of tumble was conducted recently by Salazar and Kaiser [43]; this has shown flame centroid speeds for $\phi = 0.25$ to be relatively constant and of the order 3–5 m/s throughout the first 5° CA AIT for homogeneous mixture preparation; for DI operation respective velocities throughout the same crank-angle window were of the order 8–15 m/s (with the highest values measured within the first 1.5° CA AIT). Low tumble showed consistently ~2 m/s lower flame centroid speeds than the high tumble case for both mixture preparation strategies. Considering that the engine of the current study had a configuration that was more akin to the low tumble configuration of [43], the primary differences can be attributed to the plane of visualization, engine load, as well as differences in ϕ. Further work is needed in this area for more definitive statements and comparisons, as there is always some ambiguity associated with discrimination between the balance of a flame centroid of area being at a specific in-cylinder location due to flame 'convection' by the flow field or due to preferential flame propagation from fuel concentration and temperature field effects.

The main focus in the next section will be on quantitative analysis of flame growth rates for the two fuels. Gasoline is presented first and mostly as a benchmark fuel in the same geometry to set the scene in comparison to other studies in the literature and most importantly to put the results of hydrogen's combustion speeds into perspective.

3.1.2. *Gasoline*

Fig. 5 and Fig. 6 present plots of flame radii (R) and flame expansion speeds (dR/dt), respectively. By observing the flame radii, it is noted that flame growth was more sensitive to the quality of the mixture rather than to the mixture preparation method employed. In reaching the size of the optical bore, the DI $\phi = 1.0$ curve shows more accentuated gradients when compared to the same mixture prepared by PFI. This could be attributed to fuel stratification and locally richer regions encountered by the flames travelling towards the cylinder walls when the engine was operated with DI. The highest peak in flame speed of ~12 m/s was achieved with stoichiometric DI. Both DI and PFI flames at all conditions consistently accelerated during the first 7–20° CA AIT with a short 'plateau' between 10 and 15° CA AIT for DI conditions. It needs to be pointed out that the decrease in speed from ~20–25° CA AIT

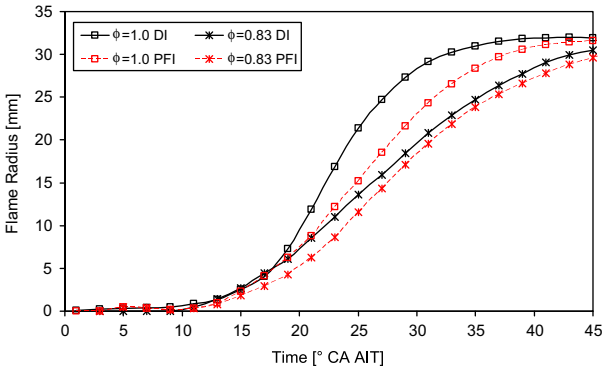

Fig. 5 – Flame Radius: Gasoline, Spark Advance 35° CA.

onwards is primarily due to masking effects by the optical crown. Therefore, the maximum values shown in Fig. 6 refer to early stages of combustion; within the first 25° CA AIT, heat release analysis showed that, typically, only ~5% of the fuel mass had been burned. This was confirmed by estimating the enflamed volume from the measured equivalent radius of Fig. 5 and transforming it to an equivalent mass based on the density of the burned gas.

The flame speeds calculated were generally in agreement with trends of other studies. For example, Serras-Pereira *et al.* [38] with a multi-hole central DI system reported values of flame growth speed of ~12 m/s for gasoline and ~11 m/s for *iso*-octane at $\phi = 1.0$ with 0.5 bar intake pressure at 1500 RPM. Aleiferis *et al.* [40] also calculated values of gasoline flame speeds of ~12 m/s with a slightly different injection system to that of [38], but at the same operating conditions. The relatively slower combustion ascertained by the current authors are attributed to synergies between the larger fraction of residuals, lower compression ratio of the engine in use, as well as lower engine speed (turbulent intensity scales with the latter). It has not been easy to pinpoint other studies that have reported flame expansion speeds with gasoline at 1000 RPM. Beretta *et al.* [44] carried out high-speed natural light imaging in a single-cylinder optical engine of similar bore and stroke (bore 88.9 mm and stroke 101.6 mm) to that used in the current study, however with a wedge-shape combustion chamber and side mounted spark plug (hence flame propagation occurred largely in one direction across the combustion chamber).

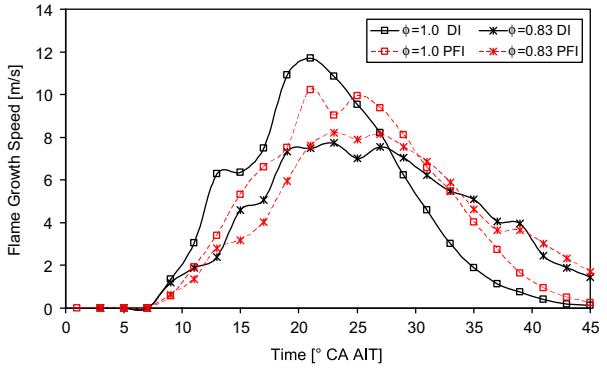

Fig. 6 – Flame Growth Speed: Gasoline, Spark Advance 35° CA.

Those tests were carried out at 1044 RPM, $\phi = 0.98$ and wide-open-throttle with 30° CA spark advance and 0.2 residual fraction, giving a pressure at ignition timing of ~7.2 bar and temperature of 570 K. The conditions at ignition timing in the current study were ~4 bar and 450 K. Using iso-octane fuelling, Serras-Pereira *et al.* [44] measured peak flame front expansion speeds of ~12 m/s at ~5° CA BTDC, corresponding to ~10% MFB. The results in Fig. 6 showed that for the fastest burning mixtures, peak flame expansion speeds of ~12 m/s were also calculated in the current study which is practically faster than the work of [44], considering the differences in in-cylinder conditions at ignition timing. The peak value was also achieved ~10° CA earlier during the experiments of Fig. 6, corresponding to ~3–5% MFB. The differences can be attributed to the 'faster-burn' pentroof combustion chamber design of the current engine with centrally located spark plug.

To put those in-cylinder burning rates in perspective, reference to turbulent burning velocities from the literature can be useful. Lawes *et al.* [45], using Schlieren imaging, calculated turbulent burning velocities for various fuels from explosions in a closed vessel with u′ = 2 m/s, 20 mm integral length scale, at 5 bar and 360 K. They reported values of ~0.9 m/s for stoichiometric iso-octane flames of ~30 mm in diameter, determined through Schlieren imaging. The burning speeds for equivalent-sized flames in the current study were calculated but, in order to make meaningful comparisons, it was necessary to take into account the differences in the integral lengths scale between the engine and the combustion bomb used by Lawes *et al.* [45]. The integral length scale in the engine was calculated on the basis of the original work of Fraser and Bracco [46] whose results have been verified by various researchers using flow-field measurements in various engines since. Specifically, Fraser and Bracco [46] found that the longitudinal integral length scale (in the cylinder axis) scaled with the clearance height by a factor of ~0.1–0.15 from 310° to 360° CA ATDC in the compression stroke. Using the instantaneous cylinder volume from 300° to 360° CA ATDC for the current engine, an 'equivalent' clearance height was calculated by dividing by the cylinder bore area, from which an integral length scale could be obtained. These scales were calculated to be ~6 mm at 15° CA AIT reducing to ~1.25 mm at TDC. Thus flames with radii of 3–4 mm were used to calculate burning velocities from the flame growth speeds of Fig. 6 by dividing with the ratio of unburned to burned gas densities (from GASEQ [47] using iso-octane's properties). For PFI, values of ~0.7 m/s burning velocity were calculated with $\phi = 0.83$ and ~1.1 m/s for $\phi = 1$. Turbulent burning velocity data for gasoline and iso-octane were available from the Leeds Combustion Group [48] and given as ~1.05 m/s and ~0.9 m/s at stoichiometry, respectively; laminar burning velocities for $\phi = 1.0$ were ~0.31 m/s and ~0.29 m/s, respectively (all without residuals). At $\phi = 0.83$ the laminar burning velocities of gasoline and iso-octane from [45] were almost identical and equal to ~0.25 m/s; the turbulent burning equivalents were ~0.8 ms/s and ~0.62 m/s, respectively. Therefore, nominally, burning velocities in the engine were calculated to be roughly similar to those in the closed vessel. However, the presence of residuals in the engine had an impact on the laminar burning velocities; typically, for 0.22 residual gas fraction, the laminar burning velocity is ~60% that without residuals at the same conditions of ϕ, pressure and temperature [49]. Taking this into account, the burning velocities in the engine were actually higher than their combustion bomb equivalent values. It should also be borne in mind that in the bomb, flames only grew to ~3 times the integral length scale, whereas in the engine, flames can grow to more than 30 times the integral length scale, so the turbulent burning velocity increases in an engine during flame propagation to much greater values than one would get in a combustion bomb experiment similar to [45,48]. Possible stratification of the charge affecting the local equivalence ratio and the presence of droplets in the mixture field would also contribute to a further increase in the burning rates as demonstrated in Bradley *et al.* [50]. However, at the early stages of combustion, when the flame was about 1.5 mm in radius, the burning speed calculated from Fig. 6 was ~0.35 m/s, *i.e.* quite close to the laminar burning speed of gasoline quoted earlier.

3.1.3. *Hydrogen*

Fig. 7 and Fig. 8 present flame radii and expansion speeds for hydrogen at different equivalence ratios with DI and PFI. The DI flame filled the optical crown at about 5–6° CA AIT, as opposed to PFI where similar sizes were depicted at ~11–12° CA AIT. A comparison between hydrogen's DI flame images in the range 4–7° CA AIT for $\phi = 0.83$ and $\phi = 0.67$ demonstrates that there is about 1–1.5° CA delay in reaching the same flame size for the leaner case of the two. For PFI, the delay is consistently of the order 2° CA within the time period of 5–10° CA AIT. Such a marked difference between injection modes can be attributed to some main sources: larger degree of stratification brought by the internally formed mixture (especially when considering the large gradient of hydrogen's laminar flame with ϕ), differences in in-cylinder motion induced by the hydrogen jets, as well as the in-cylinder thermodynamic conditions at ignition timing. The latter was observed from pressure traces where in-cylinder pressure higher by ~1 bar was present at ignition timing for DI hydrogen operation due to the large injected fuel mass under closed-valve injection strategy; potential effects of this could be contributing to enhanced early combustion speeds from further flame cellularity effects and/or different gas temperatures. Proper estimation of the in-cylinder gas temperature with DI operation requires consideration of hydrogen's

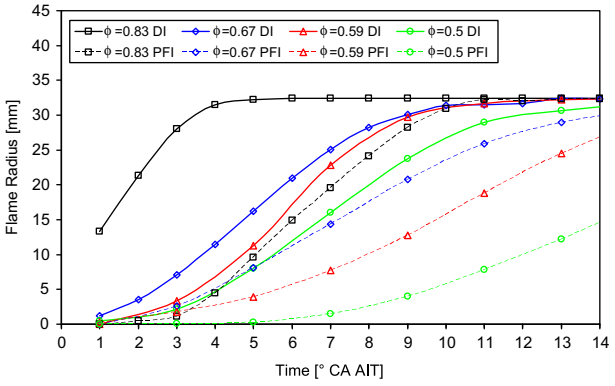

Fig. 7 – Flame Radius: Hydrogen, Spark Advance 15° CA.

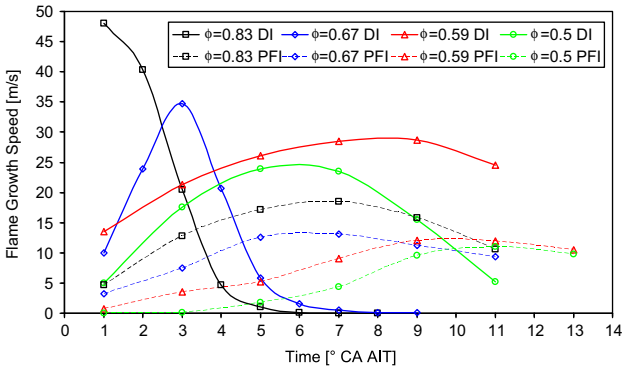

Fig. 8 – Flame Growth Speed: Hydrogen, Spark Advance 15° CA.

negative Joule-Thomson coefficient; this is currently being studied by thermodynamic modelling and Computational Fluid Dynamics (CFD) and will be reported in a future publication. In Fig. 8 it is also interesting to note how the richest DI mixture with $\phi = 0.83$ yielded a decreasing curve with maximum of ~45 m/s at the start (1–2° CA AIT). In contrast, the $\phi = 0.67$ DI mixture showed a curve with increasing trend up to ~3° CA AIT and a change in the sign of the gradient from there on; this means that for $\phi = 0.83$ higher temporal resolution would be beneficial within the first 2° CA AIT to capture a possible ascending trend in flame expansion speed similarly to that captured for the $\phi = 0.67$ case.

In-cylinder hydrogen flame expansion speed measurements have also been reported by Meier *et al.* [20] using high-speed Schlieren photography. These authors employed a single-cylinder optical engine with side combustion chamber and with both internal and external mixture formation. Direct comparison is not straightforward because it is certain that the side combustion chamber produced quite different in-cylinder 'mean' flow and turbulence characteristics than the pentroof engine used for the current study. However, upon comparison it was observed that the peak flame expansion speeds were not that dissimilar between the two studies. For example, with internal mixture formation at an un-throttled engine speed of 1000 RPM with spark advance of 5° CA and $\phi = 0.5$, a value of ~35 m/s was measured at 0.2 ms AIT, that dropped steadily to levels of ~10 m/s at 1 ms AIT. For external mixture formation, the respective values were 18 m/s at 0.2 ms AIT and 15 m/s at 1 ms AIT. In a pentroof SI engine with side DI of hydrogen, White [24] measured from OH chemiluminescence images flame expansion speeds of ~15 m/s for $\phi = 0.51$ at 1200 RPM un-throttled conditions (1 bar intake pressure). However, in the latter study, the average flame radius at a given CA was determined by fitting a bounding box to the threshold ensemble-averaged image and the average flame radius was defined as one-half of the square root of the area A of the bounding box (*i.e.* $R = 0.5A^{1/2}$), hence direct comparison with the current study can be misleading; however, on the basis of methodology, differences not really more than 10–15% should be expected between the 'equivalent' radius of the current study and that of White [24]. Indeed, considering flame expansion speeds at $\phi = 0.5$ in the range ~10–25 m/s for DI in the current study, the differences between White [24], Meier *et al.* [20] and Fig. 8 can be considered small. At the same rotational speed to that of White [49], 1200 RPM, but in a square-piston optical engine geometry with $\phi = 1.0$ and 0.5 bar intake pressure, Heywood and Vilchis [17] measured by Schlieren imaging ~16 m/s flame expansion speeds at ~9° CA AIT, with almost linear rate of increase from ~5 m/s at 3° CA AIT. On this occasion, the ~20 m/s expansion speed calculated for PFI with $\phi = 0.83$ in the current study can be partially explained by the lower compression ratio of the square-piston engine of [17] and, most probably, by large differences in in-cylinder flow fields at ignition timing, despite the lower residual gas fraction in [17]. Finally, in a pentroof engine with PFI hydrogen, Kirchweger *et al.* [22] calculated from fuel-tracer LIF images (using TEA, TriEthylAmine as fuel dopant) flame speeds on a central vertical engine plane by means of the radius of the boundary between burned and unburned mixtures (at a location parallel to the pentroof walls). The engine was 499 cc and it was run at 1000 RPM, part-load, with $\phi = 1$, $\phi = 0.67$ and $\phi = 0.5$, hence quite similar conditions to those of the current study. The calculated speeds were constant from the onset of combustion: 30.2 m/s for $\phi = 1.0$ (measured from 0.2 to 1.0 ms AIT, *i.e.* from ~1.2–6° CA AIT), 18.9 m/s for $\phi = 0.67$ (from 0.2 to 1.7 ms AIT, *i.e.* from ~1.2–10° CA AIT) and 12.5 ms for $\phi = 0.5$ (from 0.2 to 2.5 ms AIT, *i.e.* from ~1.2–15° CA AIT). Those expansion speeds can be compared to the speeds derived by the current study after considering differences in valve timings (60° CA valve overlap in [22], hence lower residual gas fraction). Specifically with PFI in Fig. 8, at $\phi = 0.67$ the flame expansion speed ranged from ~6 m/s at 1° CA AIT to ~10 m/s at 10° CA AIT, with peak of ~16 m/s at ~5° CA AIT; at $\phi = 0.5$ the speed peaked at about 15 m/s at 11° CA AIT, with values close to 10 m/s on average for most of the period 9–14° CA AIT. This suggests that the $\phi = 0.67$ mixture was probably affected comparatively more by the increased residual gas fraction than the $\phi = 0.5$ mixture, but overall the values are in agreement with those of [22].

Using similar methodologies to those described for gasoline in the previous section, the initial burning speed for hydrogen flames of 1.5–2 mm radius were calculated to range from ~2 m/s for DI mixtures at $\phi = 0.67$ down to ~0.22 m/s for the leanest PFI mixture of $\phi = 0.5$. The peak values reached ~10 m/s for the richer DI flame ($\phi = 0.83$) which after 1° CA only had already a flame radius of 13.5 mm. Whilst the highest values are not comparable to those obtained for hydrocarbon flames by this and previous authors, by adjusting global ϕ and mixture formation strategy, it is possible to control hydrogen to fire with speeds similar to those of stoichiometric hydrocarbons, especially under conditions of high residual gas dilution (*e.g.* to avoid knocking). This is demonstrated mainly by the leaner PFI mixtures, *i.e.* $\phi = 0.67$ and $\phi = 0.5$ which did not surpass 15 m/s, as shown in Fig. 8, *i.e.* comparable with those found for gasoline during the earlier tests.

Laminar burning velocities of hydrogen presented in [30,31] were found to reach values of ~6 m/s for ignition temperatures of 500 K with $\phi = 1.0$ at 1 bar. Furthermore, an increase in pressure from 1 bar to 5 bar in [30] with $\phi = 0.5$ at 365 K led to laminar burning velocities of ~0.5–0.6 m/s. It needs to be noted here that due to the high mass diffusivity of hydrogen, lean to stoichiometric hydrogen/air mixtures will be diffusionally unstable; experimental data [31] have shown

hydrogen/air flames at 1 bar to be associated with positive Markstein numbers close to stoichiometry, but for $\phi < 1.0$ negative Markstein numbers are obtained as soon as the pressure at ignition exceeds about 4 bar. This implies that hydrogen flames at engine-like conditions are unstable and will be cellular from inception and it is not really possible to measure stable laminar burning velocities directly, hence experimental derivation of stretch-free burning velocities results in decreased accuracy. Critical flame radii for the onset of instability have been found to be in the range 2.5–5 mm for 5 bar, decreasing to ~0.5–1.5 mm for 10 bar [30], hence the 'laminar flamelets' are supposed to be cellular from almost inception throughout the current study. Verhelst *et al.* [51] derived a correlation for the laminar burning velocity u_l in order to account for effects of pressure (p), equivalence ratio (ϕ), temperature (T) and fraction of residuals (f). Exponents were empirically derived for T/T_0 and p/p_0 by studying sufficiently large flames ($R = 10$ mm) in order to obtain values of u_l to compare with u_{l0} at different operating conditions of T, p and f. The effect of residuals was incorporated specifically for engine-like conditions ($p_0 = 5$ bar, $T_0 = 365$ K, hence 'stretched' conditions) by multiplying the laminar burning velocity by $(1-\gamma f)$, where f the residual gas content in volume fraction and $\gamma = 2.715–0.5\phi$. Therefore, for $\phi = 0.5–1.0$ and a residual fraction of 0.22, this leads to laminar burning velocities ~50–60% those with no residual gas fraction.

In [51] laminar burning velocities were found to reach peak values of ~5–6 m/s at $\phi = 1$, 500 K, 5 bar, or ~2 m/s at conditions more akin to the current study ($\phi = 0.85$ at 5 bar, 365 K). The maximum values achieved by the turbulent flames monitored during the current experiments were found to be as high as ~10 m/s for the richest mixture of $\phi = 0.83$. For weak to moderate turbulence, it is well known that the turbulent burning velocity u_t increases with the turbulent intensity u' due to the increased flame surface area from turbulent wrinkling. Specifically, for very low u', the ratio u_t/u_l increases almost linearly with the ratio u'/u_l. For stronger turbulence the turbulent burning velocity u_t increases less and can even decrease by increasing quenching due to excessive stretch. Numerous combustion models assume that the turbulent motion 'erases' the flame instabilities so that these have no effect on the turbulent burning velocity, while others assume that instability effects are only felt at low u'/u_l. Verhelst [52] tested hydrogen flames at $u' = 1$, 2, 4 and 6 m/s and the figures he reported are in some agreement with the data collected by the current authors. Specifically, at 5 bar and 365 K, values of turbulent burning velocity for flames three times the integral length scale in the combustion bomb (*i.e.* 30 mm in diameter) at $\phi = 0.6–0.8$ were found to be in the range 6–7 m/s when u' was set to 4 m/s and 3–5 m/s when u' was set to 2 m/s. Levels of in-cylinder turbulence at ignition timing were expected in the range 3–4 m/s on the basis of PIV and LDV measurements in engines of similar geometry [53]. Hydrogen mixtures with $\phi = 0.83$ and 0.59 fired inside the engine with burning velocities of up to 10 m/s and 6 m/s, respectively, when using DI. On the basis of similar thermodynamic conditions at ignition timing, ~5 bar and ~450 K (higher temperature than the combustion 'bomb' but effect compensated by the presence of residuals in the engine), and u' in the range 2–4 m/s, the burning velocity values derived from the current imaging data were higher than those measured in the combustion bomb. This can be attributed to the mixture preparation method and locally rich pockets of hydrogen, because with PFI the burning velocities were typically ~50% lower than with DI and close to those measured in the combustion bomb with $u' = 2$ m/s.

Finally, an attempt was made to quantify the degree of flame stretch from the current set of data. The flame stretch rate, α, is defined as the time derivative of the area, A, of an infinitely small flame element, divided by the total area, $(1/A)(dA/dt)$; for spherically propagating flames, the stretch is $(2/R)(dR/dt)$. Photographic measurements of propagating flames can allow calculation of a 'measure of flame stretch' by the use of the equivalent flame radius R. The results are shown in Fig. 9. All conditions showed very high levels of flame stretch from the point of ignition but once the flames had grown to sizes of the order 5–10 mm in radius levels of stretch were measured to be in the range 5000–10,000 s^{-1}. To put those values into perspective, it is worth pointing out that Bradley [29] presented extinction rates of 2000 s^{-1} for hydrogen laminar flames at $\phi = 0.50$ and of 500 s^{-1} for *iso*-octane laminar flames at $\phi = 1.0$, both at conditions of 1 bar, 298 K. There is clearly a need for measurement of extinction stretch rates at engine-like conditions in the controlled environment of a combustion bomb in order to discuss differences with values measured in the engine.

3.2. *OH Laser induced fluorescence*

Fig. 10 shows images of OH LIF with hydrogen fuelling at different equivalence ratios; crank-angle timings have been selected to illustrate flames of similar sizes. Overall, the OH distribution developed throughout the cycle quite symmetrically from the spark plug to the cylinder walls, as also recorded in the earlier images of broadband flame chemiluminescence. Typical images of this type of behaviour are shown in the first row of hydrogen flames in Fig. 10. However, small-scale wrinkling and large-scale distortion of the flame-front structure was clear in some of the OH images acquired on a cycle-by-cycle basis; some of these have been included in Fig. 10. For comparison, a series of OH images from *iso*-octane combustion at $\phi = 0.83$ is also shown in Fig. 10. The large degree of wrinkling and irregularity in shapes from cycle to cycle is in direct contrast to the OH maps of hydrogen's combustion.

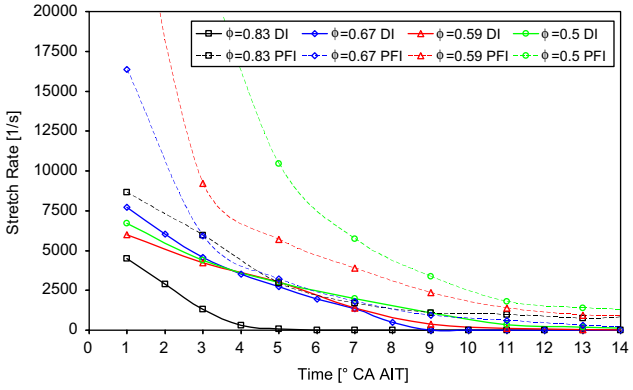

Fig. 9 – Flame Stretch: Hydrogen, Spark Advance 15° CA.

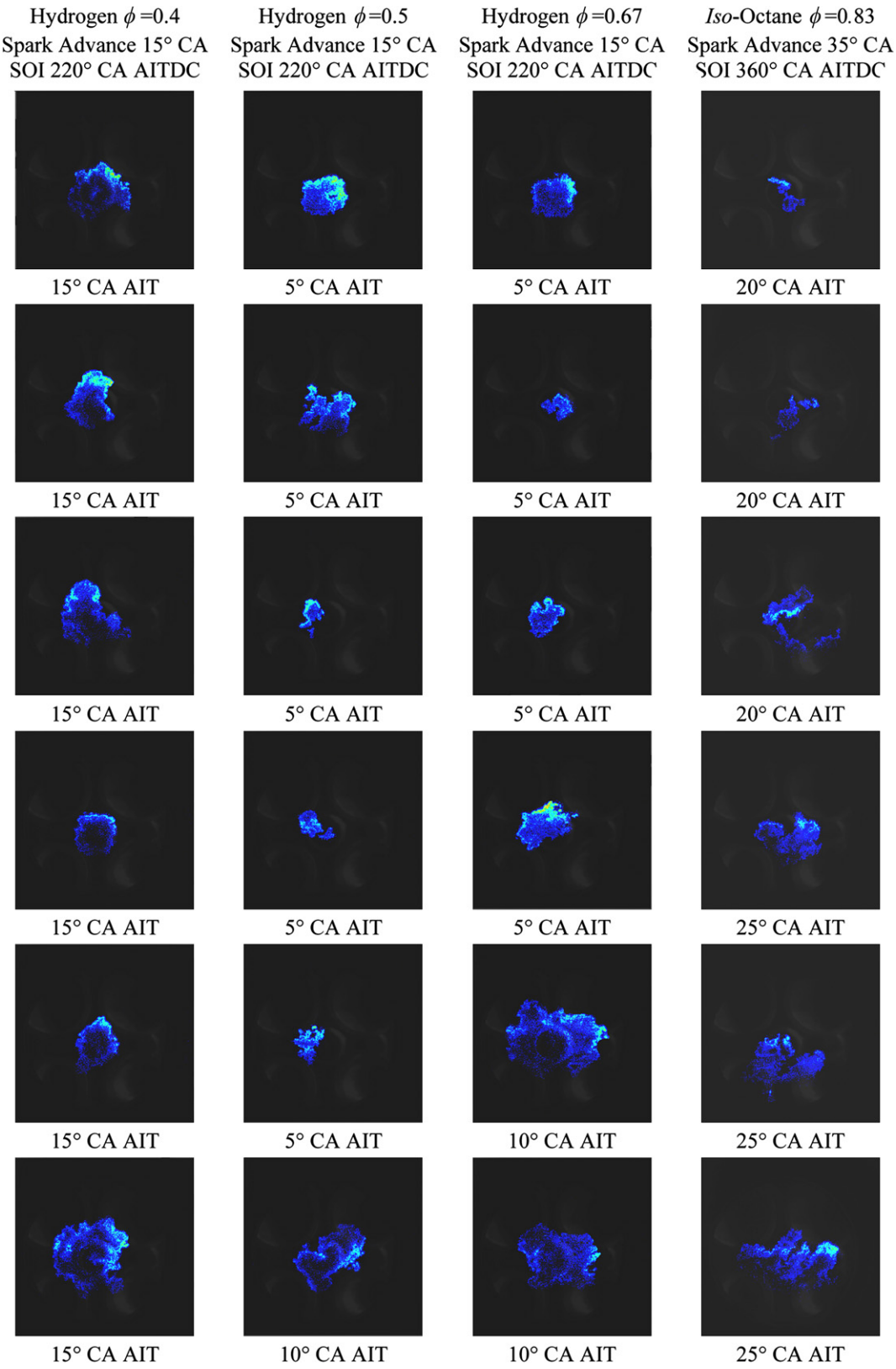

Fig. 10 – OH LIF: Hydrogen (DI); *Iso*-Octane (PFI) (Intake Valves at the Top, Exhaust Valves at the Bottom).

The literature is very scarce on high-pressure high-temperature turbulent hydrogen flames, hence linking the current data with such effects in 'controlled' turbulent conditions, like those in combustion 'bombs' is not straightforward. Measurements from combustion bombs have shown that positive stretch rates have a stabilising effect on the

flame only for positive Markstein numbers. At 1 bar, positive Markstein values are associated with hydrogen mixtures richer than $\sim\phi = 0.6$ [27], hence leaner mixtures than those are expected to be more sensitive to disturbances. However, when pressure is increased to 5 bar, there is a double effect on combustion dynamics: higher pressure leads to reduced Karlovitz factors, thus to a diminished stabilising effect of stretch on the flame, and simultaneously to reduced Markstein numbers, thus to an inverted effect of the positive stretch, especially for the leanest equivalence ratios. Specifically, at 5 bar, Markstein numbers are consistently negative throughout $\phi = 0.4–1.0$. It is quite difficult to state from the 2D nature of the OH LIF images of Fig. 10 where and when local flame front extinction occurred in the engine as lack of signal might be caused by movements of the flame in/out of the imaging plane or by actual flame front extinction. However, it was generally observed that flames with broadly same sizes at the same timings for $\phi = 0.4$ typically appeared to develop flame front fragmentation more readily than the richer mixtures of $\phi = 0.5$. Nevertheless, the degree of flame front fragmentation was nowhere near the large-scale distortion and flame front fragmentation that has been typically observed for *iso*-octane combustion in the current engine, as well as in other engines in the literature, *e.g* [54].

Considering that the influence of the hydrogen DI jets on the charge motion could not be neglected, two injection strategies were tested: apart from the 'standard' one with SOI 220° CA AITDC, a second one was used with SOI 280° CA AITDC. The former corresponded to the earliest viable timing to achieve close-valve injection conditions with the injection event completed well before ignition timing (~50° CA injection duration for $\phi = 0.5$), whilst the latter had end of injection ~25° CA BTDC, *i.e.* ~10° CA before the 'standard' spark timing of 345° CA AITDC used in the current study. It was observed that flames progressed more rapidly when later injection was employed; the intensity of OH distribution was greater and large-scale distortion of the OH maps was more pronounced than small-scale wrinkling, as shown in Fig. 11. Furthermore, the second column of Fig. 11 presents OH LIF images with spark advance 40° CA. Flame growth was faster for the larger spark advance when compared to the images at the same ϕ and timings of Fig. 10; earlier spark timing led to greater distortion over large-scales and small scales. Considering the shape of those flames it may be said that this behaviour was due to the spark occurring closer to the end of injection, hence parts of the hydrogen jets may have been ignited whilst still quite rich in fuel close the spark plug, as well as due to locally large gradients in the flow field from momentum exchange between the in-cylinder air motion and the high pressure hydrogen injection.

A comparison with the limited literature on in-cylinder hydrogen OH LIF imaging showed that in Kirchweger *et al.* [22] late hydrogen DI with SOI = 40° CA BTDC led to intense fuel stratification with high concentration of fuel on the exhaust side of the cylinder; combustion was found to take place at first in a part of the combustion chamber that corresponded to the region with the fuel rich zones. During the later stage, a zone of intensive reactions was observed in the region below the injector towards the inlet valves. It is believed that the very late injection employed in [22] led to more locally 'mixture-driven' flames, with combustion following a less symmetrical path when compared to the images of the current study. In [22] only ensemble-averaged OH LIF images were presented; these had a 'soft-focus' effect at the edges of the flame due to cyclic variability and no direct comparison could be made with the cyclically-resolved OH LIF images of the present study. Quantitative analysis on the degree of wrinkling and large-scale distortion of the OH flames is currently in progress based on methods in [55], and will be reported in a future publication.

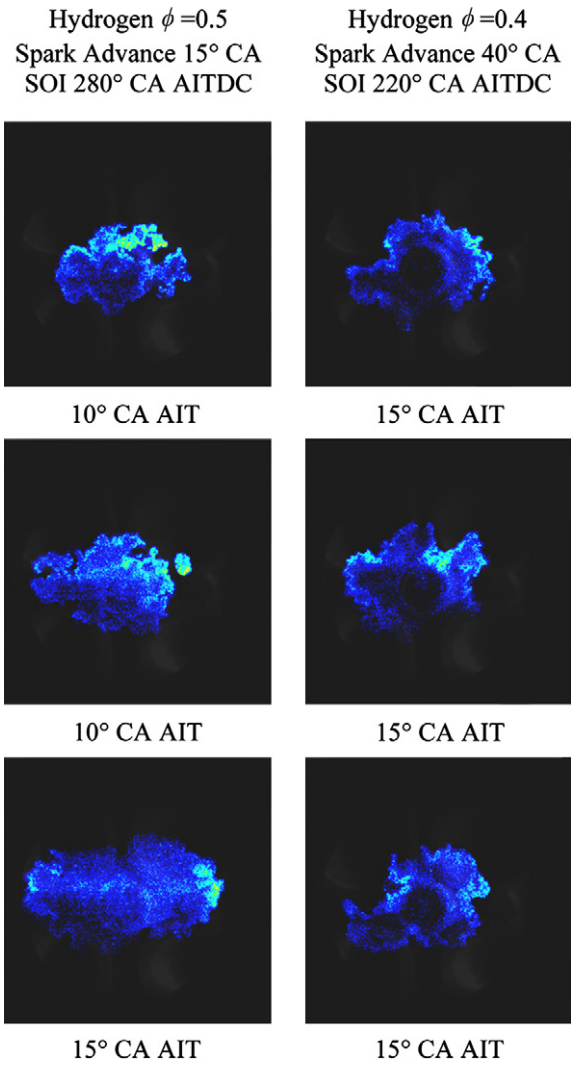

Fig. 11 – OH LIF: Hydrogen (DI), SOI 220° & 280° CA AITDC, Spark Advance 15° CA & 40° CA (Intake Valves at the Top, Exhaust Valves at the Bottom).

4. Summary and conclusions

The current paper presented results from an optical study of combustion of hydrogen in a spark-ignition engine. The engine speed was fixed to 1000 RPM with 0.5 bar intake pressure and was run with both direct injection and port injection of hydrogen and gasoline for comparison. Crank-angle resolved flame chemiluminescence images were post-

processed to infer rates of flame growth for each test case. Laminar and turbulent burning velocity data were collected from the literature at engine relevant conditions to make further comparisons and aid interpretation of the results. Analysis was also carried out by Laser Induced Fluorescence of OH. The main conclusions of this study can be summarised as follows:

- Spark ignition of hydrogen exhibited a fairly symmetrical flame growth on a macro-scale, over the range of AFR tested ($\phi = 0.50–0.83$) for both PFI and DI mixture formation strategies. This was in direct contrast to gasoline's behaviour.
- Hydrogen' peak flame expansion speeds for DI operation were in excess of 35 m/s for $\phi = 0.67–0.83$ and remained in the range 25–30 m/s for $\phi = 0.50–0.59$. For PFI operation, hydrogen combustion was much slower with measured peak expansion speeds in the range 10–20 m/s for $\phi = 0.50–0.83$.
- Gasoline peak flame expansion speeds were measured in the range 8–12 m/s for $\phi = 0.83–1.0$, with differences between DI and PFI of ~10%. Gasoline flames of 2–3 mm were used to calculate burning velocities from the flame growth speeds and burned/unburned gas density ratios. Values in the range 1.1–1.5 m/s were derived for the fastest burning mixtures.
- Hydrogen's burning velocity was derived to have values of up to 10 m/s with DI. These values were found to be higher than turbulent burning velocities measured in enclosed vessels with turbulence intensity of the order 4 m/s, especially when considering the presence of residual gases in the engine. The differences can be related to mixture preparation under DI operation because with hydrogen PFI the burning velocities derived from the current set of data were close to those obtained from combustion vessels with turbulence intensity of 2 m/s.
- A measure of flame stretch was calculated from the equivalent flame radii and expansion speeds and this was found in the range 5000–10,000 s^{-1} for early flames up to 5 mm in radius.
- OH LIF images showed that, although flames had symmetric expansion in typical cycles, some cycles did exhibit distorted shapes on a macro-scale along with presence of small-scale wrinkling. Such effects were mainly observed at equivalence ratios around $\phi = 0.50$, but the overall fragmentation and cyclic variability was not anywhere close to the levels observed in the OH images of iso-octane flames at $\phi = 0.83$.
- Adjusting the injection timing to occur closer to ignition timing by either retarding the start of injection or advancing the spark timing, showed faster flame growth. The intensity of OH distribution was greater with more pronounced large-scale distortion when later injection was employed, whilst earlier spark timing led to even greater distortion over large-scales and small scales.

Further work would be beneficial with simultaneous OH LIF and PIV, along with numerical simulation of mixture formation using real-gas thermodynamics. Experiments of hydrogen injection and combustion with controlled levels of turbulence at high pressure/temperature are needed to decouple underlying mechanisms.

Acknowledgments

The authors would like to thank the Engineering and Physical Sciences Research Council (EPSRC) in the UK for financial support (grant EP/C520211/1) and Yasunori Shimada from KEIHIN Europe for supplying the hydrogen port fuel injectors. The EPSRC instrument pool is also gratefully acknowledged for provision of the ICCD camera.

REFERENCES

[1] Norbeck JM, Heffel J, Durbin T, Montano M, Tabbara B, Bowden J. Hydrogen fuel for surface transportation. Warrendale, PA, USA: SAE; 1996.
[2] White CM, Steeper RR, Lutz AE. The hydrogen-Fueled internal combustion engine: a technical review. International Journal of Hydrogen Energy 2006;31: 1292–305.
[3] Verhelst S, Sierens R, Verstraeten S. A critical review of experimental research on hydrogen fueled SI engines. SAE; 2006. Paper 2006-01-0430.
[4] Verhelst S, Verstraeten S, Sierens R. A comprehensive overview of hydrogen engine design features. Proceedings of IMechE, Part D, Journal of Automobile Engineering 2007;221: 911–20.
[5] Verhelst S, Wallner T. Hydrogen-fuelled internal combustion engines. Progress in Energy and Combustion Science 2009;35: 490–527.
[6] Das LM. On-board hydrogen storage systems for automotive application. International Journal of Hydrogen Energy 1996; 21:789–800.
[7] Karim GA. Hydrogen as a spark ignition engine fuel. International Journal of Hydrogen Energy 2003;28:569–77.
[8] Cracknell RF, Alcock JL, Rowson JJ, Shirvill LC, Üngüt A. Safety considerations in retailing hydrogen. SAE; 2002. Paper 2002-01-1928.
[9] Li H, Karim GA. An experimental investigation of SI engine operation on gaseous fuels lean mixtures. SAE; 2005. Paper 2005-01-3765.
[10] Heffel JW. NO_x emission and performance data for a hydrogen fueled internal combustion engine at 1500 RPM using exhaust gas recirculation. International Journal of Hydrogen Energy 2003;28:901–8.
[11] Heffel JW. NO_x emission and performance data for a hydrogen fueled internal combustion engine at 3000 RPM using exhaust gas recirculation. International Journal of Hydrogen Energy 2003;28:1285–92.
[12] Verhelst S, De Landtsheere J, De Smet F, Billiouw C, Trenson A, Sierens R. Effects of supercharging, EGR and variable valve timing on power and emissions of hydrogen internal combustion engines. SAE; 2008. Paper 2008-01-1033.
[13] Nande AM, Szwaja S, Naber JD. Impact of EGR on combustion processes in a hydrogen fuelled SI engine. SAE; 2008. Paper 2008-01-1039.
[14] Welch A, Mumford D, Munshi S, Holbery J, Boyer B. Challenges in developing hydrogen direct injection technology for internal combustion engines. SAE; 2008. 2008-01-2379.
[15] Verhelst S, Sierens R. Combustion studies for PFI hydrogen IC engines. SAE; 2007. Paper 2007-01-3610.
[16] Wallner T, Lohse-Busch H. Performance, efficiency and emissions evaluation of a supercharged, hydrogen-powered, 4-cylinder engine. SAE; 2007. Paper 2007-01-0016.

[17] Heywood JB, Vilchis FR. Comparison of flame development in SI engine fuelled with propane and hydrogen. Combustion Science and Technology 1984;38:313–24.
[18] Meier F, Wiltafsky G, Köhler J, Stolz W. Quantitative time resolved 2D fuel-air ratio measurements in a hydrogen direct injection SI engine using spontaneous Raman scattering. SAE; 1996. Paper 961101.
[19] Koyanagi K, Hiruma M, Yamane K, Furuhana S. Effect of hydrogen jet on mixture formation in a high-pressure injection hydrogen fuelled engine with spark ignition. SAE; 1993. Paper 931811.
[20] Meier F, Köhler J, Stolz W, Bloss WH, Al-Garni M. Cycle-resolved hydrogen flame speed measurements with high-speed Schlieren technique in a hydrogen direct injection SI engine. SAE; 1994. Paper 942036.
[21] Blotevogel T, Egermann J, Goldlücke J, Leipertz A, Hartmann M, Schenk M, Berckmüller M. Developing planar laser-induced fluorescence for the investigation of the mixture formation process in hydrogen engines. SAE Paper, 2004-01-1408.
[22] Kirchweger W, Haslacher R. Applications of the LIF method for the diagnostics of the combustion process of gas-IC-engines. Experiments in Fluids 2007;43:329–40.
[23] White CM. A qualitative evaluation of mixture formation in a direct-injection hydrogen-fuelled engine. SAE; 2007. Paper 2007-01-1467.
[24] White CM. OH* chemiluminescence measurements in a direct-injection hydrogen-fuelled internal combustion engine. International Journal of Engine Research 2007;8:185–204.
[25] Salazar VM, Kaiser SA. An optical study of mixture preparation in a hydrogen-fuelled engine with direct injection using different nozzle designs. SAE; 2009. Paper 2009-01-2682.
[26] Salazar VM, Kaiser SA. Influence of the in-cylinder flow field (Tumble) on the fuel distribution in a DI hydrogen engine using a single-hole injector. SAE; 2010. Paper 2010-01-0579.
[27] Kaiser S, White CM. PIV and PLIF to evaluate mixture formation in a direct-injection hydrogen-fuelled engine. SAE; 2008. Paper 2008-01-1034.
[28] Milton BE, Keck JC. Laminar burning velocities in stoichiometric hydrogen and hydrogen-hydrocarbon gas mixtures. Combustion and Flame 1984;58:13–22.
[29] Bradley D. Combustion and design of future engine fuels. Proceedings of the Institution of Mechanical Engineers. 223 [Part C].
[30] Bradley D, Lawes M, Liu K, Verhelst S, Woolley R. Laminar burning velocities of lean hydrogen-air mixtures at pressures up to 1.0 MPa. Combustion and Flame 2007;149:162–72.
[31] Law CK, Jomaas G, Bechtold JK. Cellular instabilities of expanding hydrogen/propane spherical flames at elevated pressures: theory and experiment. Proceedings of the Combustion Institute 2005;30:159–67.
[32] Wu M-S, Kwon S, Driscoll JF, Faeth GM. Turbulent premixed hydrogen/air flames at high Reynolds numbers. Combustion Science and Technology 1990;73:327–50.
[33] Wu M-S, Kwon S, Driscoll JF, Faeth GM. Preferential diffusion effects on the surface structure of turbulent premixed hydrogen/air fames. Combustion Science and Technology 1991;78:69–96.
[34] Aung KT, Hassan MI, Faeth GM. Effects of pressure and nitrogen dilution on flame/stretch interactions of laminar premixed $H_2/O_2/N_2$ flames. Combustion and Flame 1998;112:1–15.
[35] Aung KT, Hassan MI, Kwon S, Tseng L-K, Kwon O-C, Faeth GM. Flame/stretch interaction in laminar and turbulent premixed flames. Combustion Science and Technology 2002;174:61–99.
[36] Rosati MF, Aleiferis PG. Hydrogen SI and HCCI combustion in a direct-injection optical engine. SAE International Journal of Engines 2009;2:1710–36. Paper 2009-01-1921.
[37] Lotus engine simulation software, http://www.lesoft.co.uk/index.html; 2010.
[38] Serras-Pereira J, Aleiferis PG, Richardson D, Wallace S. Mixture formation and combustion variability in a spray-guided DISI engine. Transactions of SAE, Journal of Engines 2007;116(3):1332–56. Paper 2007-01-4033.
[39] Serras-Pereira J, Aleiferis PG, Richardson D, Wallace S. Characteristics of ethanol, butanol, iso-octane and gasoline sprays and combustion from a multi-hole injector in a DISI engine. SAE International Journal of Fuels and Lubricants 2008;1:893–909. SAE Paper 2008-01-1591.
[40] Aleiferis PG, Serras-Pereira J, van Romunde Z, Caine J, Wirth M. Mechanisms of spray formation and combustion from a multi-hole injector with E85 and gasoline. Combustion and Flame 2010;157:735–56.
[41] Brunt MF, Emtage AL. Evaluation of IMEP routines and analysis errors. SAE; 1996. Paper 960609.
[42] Rosati MF. Hydrogen combustion in an optical engine. PhD thesis. University of London; 2010.
[43] Salazar V, Kaizer S. Influence of the flow field on flame propagation in a hydrogen-fueled internal combustion engine. SAE; 2011. Paper 2011-24-0098.
[44] Beretta GP, Rashidi M, Keck JC. Turbulent flame propagation and combustion in spark-ignition engines. Combustion and Flame 1983;52:217–45.
[45] Lawes M, Ormsby MP, Sheppard CGW, Woolley R. Variation of turbulent burning rate of methane, methanol, and iso-octane air mixtures with equivalence ratio at elevated pressure. Combustion Science and Technology 2005;177:1273–89.
[46] Fraser RA, Bracco FV. Cycle-resolved LDV integral length scale measurements investigating clearance height scaling, isotropy, and homogeneity in an IC engine. SAE; 1989. Paper 890615.
[47] Morley C. GASEQ: a chemical equilibrium program for Windows, http://www.gaseq.co.uk; 2005.
[48] Sheppard CGW, Lawes M. Personal communication; 2010.
[49] Metghalchi M, Keck JC. Burning velocities of mixtures of air with methanol, iso-octane and indolene at high pressure and temperature. Combustion and Flame 1982;48:191–210.
[50] Bradley D, Hicks RA, Lawes M, Sheppard CGW, Woolley R. The measurement of laminar burning velocities and Markstein numbers for iso-octane air and iso-octane-n-heptane mixtures at elevated temperatures and pressures in an explosion bomb. Combustion and Flame 1998;115:126–44.
[51] Verhelst S, Woolley R, Lawes M, Sierens R. Laminar and unstable burning velocities and Markstein lengths of hydrogen-air mixtures at engine-like conditions. Proceedings of the Combustion Institute 2005;30:209–16.
[52] Verhelst SA. Study of the combustion in hydrogen-fuelled internal combustion engines. PhD thesis. Ghent University; 2005.
[53] Malcolm JS, Behringer M, Aleiferis PG, Mitcalf J, OudeNijeweme D. Characterisation of flow structures in a direct-injection spark-ignition engine using PIV, LDV and CFD. SAE; 2011. Paper 2011-01-1290.
[54] Kashdan JT, Cherel J, Thirouard B. A study of combustion structure and Implications on post-oxidation under homogeneous and stratified operation in a DISI engine. SAE; 2006. Paper 2006-01-1262.
[55] Aleiferis PG, Taylor AMKP, Ishii K, Urata Y. The nature of early flame development in a lean-burn stratified-charge spark-ignition engine. Combustion and Flame 2004;136:283–302.